

Large Scale Structure Reconstruction with Short-Wavelength Modes: Halo Bias and Light Cone Formalism

Peikai Li,^{1,2} Rupert A. C. Croft,^{1,2} and Scott Dodelson^{1,2}

¹*Department of Physics, Carnegie Mellon University, Pittsburgh, PA 15213, USA*

²*McWilliams Center for Cosmology, Carnegie Mellon University, Pittsburgh, PA 15213, USA*

(Dated: June 3, 2020)

This is the second paper in a series where we propose a method of indirectly measuring large scale structure using information from small scale perturbations. The idea is to build a quadratic estimator from small scale modes that provides a map of structure on large scales. We demonstrated in the first paper that the quadratic estimator works well on a dark-matter-only N-body simulation at a snapshot of $z = 0$. Here we generalize our theory to the case of a light-cone with halo bias and redshift space distortions taken into consideration. We successfully apply our generalized version of quadratic estimator to a light cone halo catalog of an N-body simulation of size $\sim 5.6 (h^{-1} \text{ Gpc})^3$. The most distant point in the light cone is at a redshift of 1.4, which indicates that we might be able to apply our method to next generation galaxy surveys.

I. INTRODUCTION

Directly measuring the distribution of matter on large scales is extremely difficult right now as pointed out by [1]. The attempt to use small scale perturbations to infer large scale information has been frequently discussed in recent years [2][3][4][5][6]. In our first work [7], we proposed a method of indirectly measuring large scale structure using small scale density contrast. Physically, long- and short-wavelength modes are correlated in the sense that small scale modes will grow differently depending on the large scale structure they reside in. This phenomenon leaves a signature that the Fourier statistics of short-wavelength matter density modes will have non-zero off-diagonal terms proportional to long-wavelength modes. This is our starting point for constructing the quadratic estimator for long-wavelength modes. We tested the power of the quadratic estimator using a dark-matter-only catalog from an N-body simulation in the first paper. In this work, we generalize our theory to a halo catalog within a light cone for observational requirements.

First we need to account for halo bias [8][9] since eventually we want to apply the estimator to future cosmological surveys [10][11][12]. Halo bias is a term relating the halo number density contrast to the matter density contrast. We only consider the leading order of halo bias in this work, in consistent with the treatments of recent galaxy surveys [13][14][15]. One of the main difficulty with this generalization is that the linear halo bias is both halo redshift dependent and halo mass dependent. So we decide to build the approximate matter density contrast out of halo information, in order to break the restriction of a narrow halo mass bin if we use the halo density contrast directly.

Observationally a galaxy catalog will be in a light cone [16] instead of a snapshot. The typical treatment is to cut a light cone into several thin redshift bins [17], and analyze the properties within each bin. By doing this we will lose information about the long-wavelength modes

along line of sight. Thus in this paper we propose a novel method of considering all the halos/galaxies in a light cone together, accounting for the redshift difference by multiplying an extra factor proportional to the inverse of the linear growth function. Since the universe is linear at sufficiently large scales, linear matter density modes at different redshift will still be correlated. With this knowledge we can recover the linear power spectrum on large scales. Assuming a cube volume, we can construct the quadratic estimator for long-wavelength modes using information of non-zero off-diagonal terms as we did previously. Another observational effect we need to take into account is the redshift space distortions [18]. This effect can be straightforwardly included because redshift space's matter density contrast shares similar formalism of perturbative series as real space's.

We begin with our treatment of halo bias in a snapshot by constructing the approximate form of the matter perturbation field using the information of halo positions. We then deal with the matter density contrast in a light cone and then build the quadratic estimator. Finally we apply the estimator to different N-body simulations and successfully extract large scale modes both in a snapshot and in a light cone.

II. HALO BIAS

Let's first do a quick review of how we construct the quadratic estimator of a dark-matter-only catalog [7] before we get to a halo catalog. Starting from the perturbative series of the matter density contrast in Fourier space [19][20]:

$$\begin{aligned} \delta_m(\vec{k}; a) &= \delta_m^{(1)}(\vec{k}; a) + \delta_m^{(2)}(\vec{k}; a) + \dots \\ &= \frac{D_1(a)}{D_{\text{ini}}} \delta_m^{(1)}(\vec{k}; a_{\text{ini}}) + \left[\frac{D_1(a)}{D_{\text{ini}}} \right]^2 \delta_m^{(2)}(\vec{k}; a_{\text{ini}}) + \dots (1) \end{aligned}$$

where “m” stands for matter, the superscript $i = 1, 2, \dots$ corresponds to the i -th order term of the expansion, D_1 is the linear growth function while $D_{\text{ini}} = D_1(a = a_{\text{ini}})$ is

the value of D_1 at some initial time a_{ini} , and $\delta_m(\vec{k}; a)$ is the full Fourier space matter density contrast in a snapshot when the scale factor was equal to a . By computing the off-diagonal term $\langle \delta_m^{(1)}(\vec{k}; a) \delta_m^{(2)}(\vec{k}; a) \rangle$ we can prove the following relation of the two-point function of two short-wavelength modes:

$$\langle \delta_m(\vec{k}_s; a) \delta_m(\vec{k}'_s; a) \rangle = f(\vec{k}_s, \vec{k}'_s) \delta_m^{(1)}(\vec{k}_l; a) \quad (2)$$

here \vec{k}_s and \vec{k}'_s are two short-wavelength modes and \vec{k}_l is a long-wavelength mode ($\vec{k}_s, \vec{k}'_s \gg \vec{k}_l$). They satisfy the squeezed-limit condition $\vec{k}_s + \vec{k}'_s = \vec{k}_l$ and f is given by:

$$f(\vec{k}_s, \vec{k}'_s) = 2F_2(-\vec{k}_s, \vec{k}_s + \vec{k}'_s) P_{\text{m,lin}}(k_s; a) + 2F_2(-\vec{k}'_s, \vec{k}_s + \vec{k}'_s) P_{\text{m,lin}}(k'_s; a). \quad (3)$$

Here $P_{\text{m,lin}}$ is the linear matter power spectrum and F_2 is a function particularly insensitive to the choice of cosmological parameters in a dark-energy-dominated universe [21] with expression:

$$F_2(\vec{k}_1, \vec{k}_2) = \frac{5}{7} + \frac{2}{7} \frac{(\vec{k}_1 \cdot \vec{k}_2)^2}{k_1^2 k_2^2} + \frac{\vec{k}_1 \cdot \vec{k}_2}{2k_1 k_2} \left[\frac{k_1}{k_2} + \frac{k_2}{k_1} \right]. \quad (4)$$

Eq. (2) indicates that we can estimate long-wavelength modes using small scale information with the following minimum variance quadratic estimator:

$$\hat{\delta}_m^{(1)}(\vec{k}_l; a) = A(\vec{k}_l) \int \frac{d^3 \vec{k}_s}{(2\pi)^3} g(\vec{k}_s, \vec{k}'_s) \delta_m(\vec{k}_s; a) \delta_m(\vec{k}'_s; a) \quad (5)$$

with $\vec{k}'_s = \vec{k}_l - \vec{k}_s$. The normalization factor A is defined by requiring that $\langle \hat{\delta}_m^{(1)}(\vec{k}_l; a) \rangle = \delta_m^{(1)}(\vec{k}_l; a)$, and the weighting function g is obtained by minimizing the noise. They can be expressed as:

$$A(\vec{k}_l) = \left[\int \frac{d^3 \vec{k}_s}{(2\pi)^3} g(\vec{k}_s, \vec{k}'_s) f(\vec{k}_s, \vec{k}'_s) \right]^{-1} \\ g(\vec{k}_s, \vec{k}'_s) = \frac{f(\vec{k}_s, \vec{k}'_s)}{2P_{\text{m,nl}}(k_s) P_{\text{m,nl}}(k'_s)} \quad (6)$$

where $P_{\text{m,nl}}$ is the nonlinear matter power spectrum. With this choice of the weighting function g , the Gaussian noise term is equal to the normalization factor $N(\vec{k}_l) = A(\vec{k}_l)$. And the projected detectability of a power spectrum measurement using this quadratic estimator can be written as:

$$\frac{1}{\sigma^2(k_l)} = \frac{V k_l^2 \Delta k}{(2\pi)^2} \left[\frac{P_{\text{m,lin}}(k_l)}{P_{\text{m,lin}}(k_l) + A(k_l)} \right]^2, \quad (7)$$

where V is the volume of a survey and Δk is the width of long-wavelength mode bins. We also take advantage of the fact that $A(\vec{k}_l)$ does not depend on the direction of the long mode \vec{k}_l .

So far we have finished reviewing the general formalism of the large scale quadratic estimator in a dark-matter-only catalog. Now we generalize to a halo catalog.

Ignoring higher order halo bias, the number density contrast of halos can be related to the matter density contrast at a fixed time a as [9]:

$$\delta_h(\vec{r}; a) \equiv \frac{n_h(\vec{r}; a) - \bar{n}_h(a)}{\bar{n}_h(a)} = b_1 \delta_m(\vec{r}; a) \quad (8)$$

here “h” denotes halo, n_h is the halo number density field at a given position, \bar{n}_h is the mean number density of halos and b_1 is the linear bias parameter relating halo and matter density contrasts. The linear bias b_1 is a function of halo mass and position and has been well approximated using analytical expressions [22][23]. We will use the Tinker halo bias function throughout this paper [24]. Since the linear bias b_1 depends not only on halo mass but also halo redshift, it will be more challenging for us to use δ_h than δ_m within a light cone unless we use a very narrow mass bin. Therefore we choose to build an approximate matter density contrast out of halo positions in a snapshot following [25]:

$$\delta_m(\vec{r}; a) \equiv \frac{\eta_h(\vec{r}; a) - \bar{\eta}_h(a)}{\bar{\eta}_h(a)} \quad (9)$$

where $\eta_h(\vec{r}; a)$ is the usual halo density field with each halo weighted by the inverse of its own halo bias, and $\bar{\eta}_h(a)$ is its mean value. They can be explicitly written as:

$$\eta_h(\vec{r}; a) = \sum_{i=1}^{N_h} \frac{\delta_{\text{Dg}}(\vec{r} - \vec{r}_i)}{b_1(M_i; a_i)} \Big|_{a_i=a} \quad (10)$$

$$n_h(\vec{r}; a) = \sum_{i=1}^{N_h} \delta_{\text{D}}(\vec{r} - \vec{r}_i) \Big|_a \quad (11)$$

where δ_{D} is the Dirac delta function, N_h is the total number of halos and a_i , M_i and \vec{r}_i are the cosmological growth factor, mass and position of the i -th halo, respectively. Since we consider only a fixed time in this section, we can use the simplification $b_1(M_i, a_i) = b_1(M_i)$. We can use the Cloud-in-Cell (CIC) or the Triangular Shaped Cloud (TSC) scheme [26] to smooth the sharply peaked Dirac delta function numerically¹.

We consider Eq. (9) as the general way of estimating the matter density using the information of halos/galaxies only, since in real surveys the bias can be expressed as a function of galaxy luminosity and color [27]. We will not use the halo density contrast δ_h directly, instead we will use δ_m defined in Eq. (9) as the approximate matter density contrast during the calculation of the quadratic estimator Eq. (5) both in a snapshot and in a light cone.

¹ We use the TSC scheme in this work.

III. DEMONSTRATION WITH N-BODY SIMULATION I

We test the power of the quadratic estimator using a halo catalog from a cosmological N-body simulation. We use the $z = 0$ snapshot from BigMDPL, one of the Multi-Dark cosmological simulations [28]. This simulation used a flat Λ CDM model with Planck Collaboration XVI (2014) [29] cosmological parameters. Halos were found in this catalog using *Rockstar* code [30]. We will focus on halos with masses between $2.2 \times 10^{12} h^{-1} M_\odot < M < 10^{14} h^{-1} M_\odot$ for simplicity. And we have similar results in other mass bins as well.

We use the approximate density contrast defined in Eq. (9) and it is able to perfectly capture the nonlinear matter power spectrum. Thus the projected detectability will be the same as our last work, shown in Fig. 1.

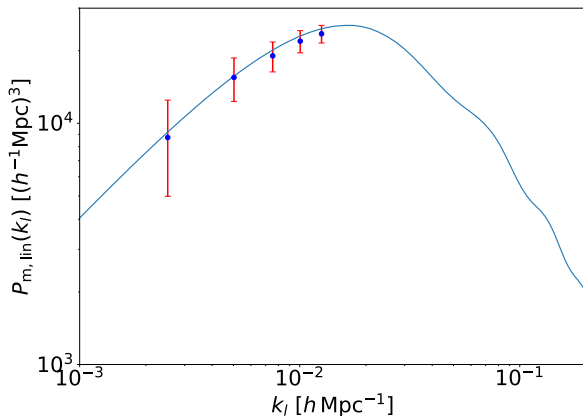


FIG. 1. Long-wavelength power spectrum and its error from Eq. (7) which can be expressed as $P_{m,lin}(k_l)\sigma(k_l)$. Boxsize of the survey is assumed to be $L = 2.5 h^{-1} \text{Gpc}$ thus volume $V = L^3$ and width $\Delta k = 2\pi/L$. The integration range for \vec{k}_s is from $0.03 h \text{Mpc}^{-1}$ to $0.22 h \text{Mpc}^{-1}$.

We also transform the true Fourier modes $\delta_m(\vec{k}_l)$ and the estimated long-wavelength modes $\hat{\delta}_m(\vec{k}_l)$ back into real space and compare them in Fig. 2. We can see that this quadratic estimator is able to successfully recapture large scale over/under densities.

IV. LIGHT CONE FORMALISM

We first define an observable, which is the modified matter density contrast in a light cone as:

$$d_m^{\text{LC}}(\vec{r}) := \delta_m(\vec{r}; a(r)) \frac{D_{\text{ini}}}{D_1(a(r))} \quad (12)$$

where “LC” stands for “light cone”. We set $a(\vec{r} = 0)$ to be the origin of the light cone. Thus $a(\vec{r}) = a(r)$ will

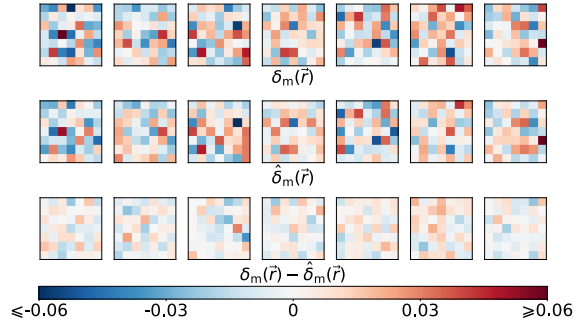


FIG. 2. Comparison of the true density field of the BigMDPL halo catalog within mass bin $2.2 \times 10^{12} h^{-1} M_\odot < M < 10^{14} h^{-1} M_\odot$ ($\delta_m(\vec{r})$ computed using the directly measured large scale modes, top row) and the density field from the quadratic estimator ($\hat{\delta}_m(\vec{r})$, middle row). The bottom row shows their difference. Each panel represents a slice through the simulation volume, $2500 h^{-1} \text{Mpc}$ wide, and one cell $\sim 357 h^{-1} \text{Mpc}$ thick. The integration range of \vec{k}_s is from $0.03 h \text{Mpc}^{-1}$ to $0.22 h \text{Mpc}^{-1}$.

not depend on the direction of position \vec{r} . The position \vec{r} runs over the whole light cone. The goal of dividing by the linear growth function is to try to set large scale amplitude the same for the whole light cone.

The field $\delta_m(\vec{r}; a(r))$ is the matter density contrast at position \vec{r} of the snapshot with scale factor $a(r)$. It can be approximated using Eq. (9) when we consider a galaxy catalog. Generally speaking, the matter density contrast $\delta_m(\vec{r}'; a(r))$ at an arbitrary position \vec{r}' is unmeasurable since observationally we cannot have direct access to a specific snapshot. While on the shell $|\vec{r}'| = |\vec{r}|$ of this snapshot, we have:

$$\delta_m(\vec{r}'; a(r)) = \frac{\rho_m(\vec{r}'; a(r')) - \bar{\rho}_m(a(r))}{\bar{\rho}_m(a(r))} \quad (13)$$

where $\rho_m(\vec{r}'; a(r'))$ is the matter density at position \vec{r}' of snapshot $a(r')$, and $\bar{\rho}_m(a(r))$ is the mean matter density of snapshot $a(r)$. In this case $\delta_m(\vec{r}'; a(r))$ is an observable since we get to know $\rho_m(\vec{r}'; a(r'))$ in cosmic surveys, since $\rho_m(\vec{r}'; a(r'))$ is the matter density field at position \vec{r}' of the light cone. And if we cut the light cone into several thin slices we are able to get a interpolation function for each value of $\bar{\rho}_m(a(r))$. Thus for each snapshot with scale factor $a(r)$, we can measure its matter density contrast $\delta_m(\vec{r}'; a(r))$ on a shell (when $|\vec{r}'| = |\vec{r}|$). Finally we come to the conclusion that the modified density contrast d_m^{LC} is an observable. The point of this construction Eq. (12) is that we know the properties of matter density contrast in a snapshot very well (e.g. Eq. (1)). And we

can take advantage of these properties to further perform our derivation. Inverse Fourier transform of the density modes in a snapshot can be written as:

$$\delta_{\text{m}}(\vec{r}; a(r)) = \int \frac{d^3\vec{k}}{(2\pi)^3} e^{i\vec{k}\cdot\vec{r}} \delta_{\text{m}}(\vec{k}; a(r)) \quad (14)$$

Again, we still do not have access to the value of the Fourier modes $\delta_{\text{m}}(\vec{k}; a(r))$. Luckily they will not show up in our final results thus our formalism can be applied in light cone simulations, and eventually surveys.

Now consider the Fourier transform of the modified density contrast within the light cone:

$$d_{\text{m}}^{\text{LC}}(\vec{k}) = \int_V d^3\vec{r} \delta_{\text{m}}(\vec{r}; a(r)) \frac{D_{\text{ini}}}{D_1(a(r))} e^{-i\vec{k}\cdot\vec{r}} \quad (15)$$

Insert the inverse Fourier transform Eq. (14) of $\delta_{\text{m}}(\vec{r}; a(r))$ into the above expression, and further break the expression Eq. (15) into perturbative series using Eq. (1). We can get:

$$d_{\text{m}}^{\text{LC}}(\vec{k}) = d_{\text{m}}^{\text{LC},(1)}(\vec{k}) + d_{\text{m}}^{\text{LC},(2)}(\vec{k}) + \dots \quad (16)$$

with each order given by:

$$d_{\text{m}}^{\text{LC},(i)}(\vec{k}) = \int_V d^3\vec{r} \int \frac{d^3\vec{k}'}{(2\pi)^3} e^{i(\vec{k}'-\vec{k})\cdot\vec{r}} \delta_{\text{m}}^{(i)}(\vec{k}'; a(r)) \frac{D_{\text{ini}}}{D_1(a(r))} \quad (17)$$

We can prove that the first order term of d_{m}^{LC} satisfies the following relation:

$$\langle d_{\text{m}}^{\text{LC},(1)}(\vec{k}) d_{\text{m}}^{\text{LC},(1)}(\vec{k}') \rangle \simeq (2\pi)^3 \delta_{\text{D}}(\vec{k} + \vec{k}') P_{\text{m,ini}}(k) \quad (18)$$

where $P_{\text{m,ini}}$ is the linear matter power spectrum at the initial time a_{ini} . This relation Eq. (18) tells us that the first order term of the modified light cone matter density contrast $d_{\text{m}}^{\text{LC}}(\vec{k})$ (which corresponds to long-wavelength modes) still characterizes the linear evolution information of the light cone, since redshift difference in the light cone has been cancelled by the extra factor $D_{\text{ini}}/D_1(a(r))$ of the integrand. Or equivalently speaking, we have $P_{\text{m}}^{\text{LC}}(k) \simeq P_{\text{m,ini}}(k)$ for long-wavelength modes (when $k \rightarrow 0$), as shown in Fig. 3. $P_{\text{m}}^{\text{LC}}(k)$ is the power spectrum of density contrast Eq. (12) defined as the diagonal term of the two-point correlation:

$$\langle d_{\text{m}}^{\text{LC}}(\vec{k}) d_{\text{m}}^{\text{LC}}(\vec{k}') \rangle \simeq (2\pi)^3 \delta_{\text{D}}(\vec{k} + \vec{k}') P_{\text{m}}^{\text{LC}}(k) \quad (19)$$

There are also off-diagonal terms in Eq. (19) which contains extremely valuable information, and we will look into them in next section V.

V. QUADRATIC ESTIMATOR

Using the expressions of Eq. (17), we can compute the two-point correlations of two short-wavelength Fourier

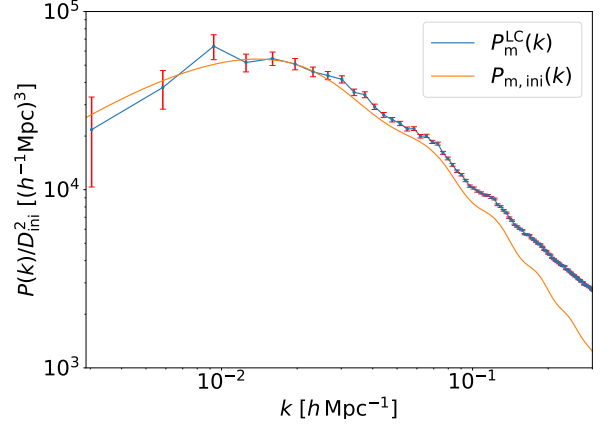


FIG. 3. Comparison of the light cone power spectrum $P_{\text{m}}^{\text{LC}}(k)$ with the initial power spectrum $P_{\text{m,ini}}(k)$, both scaled by $1/D_{\text{ini}}^2$. $P_{\text{m,ini}}(k)$ is plotted according to theory predicted linear power spectrum, and $P_{\text{m}}^{\text{LC}}(k)$ is computed using halo catalog of MICE Grand Challenge light cone simulation [31][32]. Halo mass bin is chosen to be $[2.2 \times 10^{12} h^{-1} M_{\odot}, 10^{14} h^{-1} M_{\odot}]$. They match each other pretty well on large scales ($k \lesssim 0.02 h \text{ Mpc}^{-1}$) despite tiny systematic error. The error bars shows errors due to limited number of independent modes in each bin.

modes $d_{\text{m}}^{\text{LC}}(\vec{k}_s)$ and $d_{\text{m}}^{\text{LC}}(\vec{k}'_s)$. Again we assume the squeezed limit $\vec{k}_l = \vec{k}_s + \vec{k}'_s$:

$$\begin{aligned} & \langle d_{\text{m}}^{\text{LC}}(\vec{k}_s) d_{\text{m}}^{\text{LC}}(\vec{k}'_s) \rangle |_{\vec{k}_s + \vec{k}'_s = \vec{k}_l} \\ &= \langle d_{\text{m}}^{\text{LC},(1)}(\vec{k}_s) d_{\text{m}}^{\text{LC},(2)}(\vec{k}'_s) \rangle + \langle d_{\text{m}}^{\text{LC},(2)}(\vec{k}_s) d_{\text{m}}^{\text{LC},(1)}(\vec{k}'_s) \rangle \end{aligned} \quad (20)$$

Substituting Eq. (17) into Eq. (20) and evaluate the first bracket as an example:

$$\begin{aligned} & \langle d_{\text{m}}^{\text{LC},(1)}(\vec{k}_s) d_{\text{m}}^{\text{LC},(2)}(\vec{k}'_s) \rangle \\ &= \int_V d^3\vec{r} \int_V d^3\vec{r}' \int \frac{d^3\vec{k}}{(2\pi)^3} \int \frac{d^3\vec{k}'}{(2\pi)^3} \\ & \quad e^{i(\vec{k}\cdot\vec{r} + \vec{k}'\cdot\vec{r}') - i(\vec{k}_s\cdot\vec{r} + \vec{k}'_s\cdot\vec{r}')} \frac{D_{\text{ini}}}{D_1(a(r))} \frac{D_{\text{ini}}}{D_1(a(r'))} \\ & \quad \times \langle \delta_{\text{m}}^{(1)}(\vec{k}; a(r)) \delta_{\text{m}}^{(2)}(\vec{k}'; a(r')) \rangle \end{aligned} \quad (21)$$

We have computed $\langle \delta_{\text{m,ini}}^{(1)}(\vec{k}) \delta_{\text{m,ini}}^{(2)}(\vec{k}') \rangle$ in our previous work [7] (where $\delta_{\text{m,ini}}^{(1)}(\vec{k}) \equiv \delta_{\text{m}}^{(1)}(\vec{k}; a_{\text{ini}})$), the result gives:

$$\langle \delta_{\text{m,ini}}^{(1)}(\vec{k}) \delta_{\text{m,ini}}^{(2)}(\vec{k}') \rangle = 2F_2(-\vec{k}, \vec{k} + \vec{k}') P_{\text{m,ini}}(k) \delta_{\text{m,ini}}^{(1)}(\vec{k} + \vec{k}') \quad (22)$$

We can use this result to further determine the value of the bracket in Eq. (21):

$$\begin{aligned} & \langle \delta_m^{(1)}(\vec{k}; a(r)) \delta_m^{(2)}(\vec{k}'; a(r')) \rangle \\ &= 2 \frac{D_1(a(r))}{D_{\text{ini}}} \left[\frac{D_1(a(r'))}{D_{\text{ini}}} \right]^2 \langle \delta_{m,\text{ini}}^{(1)}(\vec{k}) \delta_{m,\text{ini}}^{(2)}(\vec{k}') \rangle \\ &= 2 \left[\frac{D_1(a(r'))}{D_{\text{ini}}} \right]^2 F_2(-\vec{k}, \vec{k} + \vec{k}') P_{m,\text{ini}}(k) \delta_m^{(1)}(\vec{k} + \vec{k}'; a(r)) \end{aligned} \quad (23)$$

where we make use of the definition of the linear growth factor $D_1(a(r))$. Plugging Eq. (23) into Eq. (21), the only r' dependent integral can be written as (here we simply choose a cube volume):

$$\int_V d^3\vec{r}' e^{-i(\vec{k}' - \vec{k}_s)\vec{r}'} \frac{D_1(a(r'))}{D_{\text{ini}}} \simeq C (2\pi)^3 \delta_D(\vec{k}' - \vec{k}_s) \quad (24)$$

since $D_1(a(r'))$ is a slowly varying function. Constant C can be further determined via integrating over \vec{k}' on both sides of Eq. (24), which gives:

$$C = \frac{D_1(a=1)}{D_{\text{ini}}} \quad (25)$$

thus:

$$\begin{aligned} & \langle d_m^{\text{LC},(1)}(\vec{k}_s) d_m^{\text{LC},(2)}(\vec{k}') \rangle \\ & \simeq 2C \int_V d^3\vec{r} \int \frac{d^3\vec{k}}{(2\pi)^3} F_2(\vec{k}, -\vec{k} + \vec{k}') P_{m,\text{ini}}(|\vec{k} - \vec{k}'|) \\ & \quad \times \frac{D_{\text{ini}}}{D_1(a(r))} e^{-i(\vec{k} - \vec{k}_s - \vec{k}')\vec{r}} \delta_m^{(1)}(\vec{k}; a(r)) \\ & \simeq 2C F_2(-\vec{k}_s, \vec{k}_s + \vec{k}') P_{m,\text{ini}}(k_s) \\ & \quad \times \int_V d^3\vec{r} \int \frac{d^3\vec{k}}{(2\pi)^3} \frac{D_{\text{ini}}}{D_1(a(r))} e^{-i(\vec{k} - \vec{k}_s - \vec{k}')\vec{r}} \delta_m^{(1)}(\vec{k}; a(r)) \\ & = 2C F_2(-\vec{k}_s, \vec{k}_s + \vec{k}') P_{m,\text{ini}}(k_s) d_m^{\text{LC},(1)}(\vec{k}_s + \vec{k}') \end{aligned} \quad (26)$$

where in the first step, we perform a redefinition of the integration dummy variable. And we use an approximation in the second step in order to get the first order term $d_m^{\text{LC},(1)}(\vec{k}_s + \vec{k}')_s$ from the integral.

Again, we have proved that with this construction in Eq. (12), we can obtain the long-wavelength modes from the off-diagonal terms of short-wavelength modes:

$$\langle d_m^{\text{LC}}(\vec{k}_s) d_m^{\text{LC}}(\vec{k}') \rangle|_{\vec{k}_s + \vec{k}'_s = \vec{k}_l} = f(\vec{k}_s, \vec{k}') d_m^{\text{LC},(1)}(\vec{k}_l) \quad (27)$$

with

$$\begin{aligned} f(\vec{k}_s, \vec{k}') &= 2C F_2(-\vec{k}_s, \vec{k}_s + \vec{k}') P_{m,\text{ini}}(k_s) \\ & \quad + 2C F_2(-\vec{k}'_s, \vec{k}_s + \vec{k}'_s) P_{m,\text{ini}}(k'_s) \end{aligned} \quad (28)$$

The quadratic estimator can be similarly formed as:

$$\hat{d}_m^{\text{LC},(1)}(\vec{k}_l) = \mathcal{A}(\vec{k}_l) \int \frac{d^3\vec{k}_s}{(2\pi)^3} g(\vec{k}_s, \vec{k}') d_m^{\text{LC}}(\vec{k}_s) d_m^{\text{LC}}(\vec{k}') \quad (29)$$

with $\vec{k}'_s = \vec{k}_l - \vec{k}_s$ and g being the weighting function. By requiring that $\langle \hat{d}_m^{\text{LC},(1)}(\vec{k}_l) \rangle = d_m^{\text{LC},(1)}(\vec{k}_l)$ we can similarly determine the normalization function \mathcal{A} :

$$\mathcal{A}(\vec{k}_l) = \left[\int \frac{d^3\vec{k}_s}{(2\pi)^3} g(\vec{k}_s, \vec{k}'_s) f(\vec{k}_s, \vec{k}'_s) \right]^{-1} \quad (30)$$

Similar to our last work, by minimizing the noise we get the expression for the weighting function g :

$$\begin{aligned} g(\vec{k}_s, \vec{k}'_s) &= \frac{f(\vec{k}_s, \vec{k}'_s)}{2P_m^{\text{LC}}(k_s) P_m^{\text{LC}}(k'_s)} \\ &= C \frac{F_2(-\vec{k}_s, \vec{k}_s + \vec{k}'_s) P_{m,\text{ini}}(k_s) + F_2(-\vec{k}'_s, \vec{k}_s + \vec{k}'_s) P_{m,\text{ini}}(k'_s)}{P_m^{\text{LC}}(k_s) P_m^{\text{LC}}(k'_s)} \end{aligned} \quad (31)$$

with this choice of g the noise term \mathcal{N} is identical to the normalization factor \mathcal{A} . And the projected detectability is defined similarly as Eq. (7):

$$\frac{1}{\sigma^{\text{LC}}(k_l)^2} = \frac{V k_l^2 \Delta k}{(2\pi)^2} \left[\frac{P_{m,\text{ini}}(k_l)}{P_{m,\text{ini}}(k_l) + \mathcal{A}(k_l)} \right]^2, \quad (32)$$

Using the quadratic estimator Eq. (29) we can use small scale information of the whole light cone (for now we only consider a cube-shaped volume) to infer large scale field of the modified matter density contrast $d_m^{\text{LC}}(\vec{r})$. According to Eq. (18), this is equivalent to large scale linear matter perturbations in the light cone.

VI. DEMONSTRATION WITH N-BODY SIMULATION II

A. Real Space

We use the MICE Grand Challenge light cone N-body simulation (MICE-GC) to demonstrate the power of the estimator in a light cone. The catalog contains one octant of the full sky up to $z = 1.4$ (comoving distance $3072 h^{-1} \text{Mpc}$) without simulation box repetition. We use the largest cube that can be fit into the octant as the region V of integration in Eq. (15), as shown in Fig. 4. This simulation used a flat ΛCDM model with cosmological parameters $\Omega_m = 0.25$, $\sigma_8 = 0.8$, $n_s = 0.95$, $\Omega_b = 0.044$, $\Omega_\Lambda = 0.75$, $h = 0.7$. We also assume $D_{\text{ini}} = 1$ throughout this section².

We first extract 1 in 700 matter particles' positions in the full the light cone of MICE-GC simulation and then focus on the largest cube within it. This corresponds to $\sim 5.14 \times 10^7$ particles in total each with

² $D_{\text{ini}} = 1$ is physically ill-defined, because the maximum value of D_{ini} is about 0.997 for a flat universe with $\Omega_m = 0.25$. But D_{ini} is simply a normalization constant and the choice of its value does not affect the feature of the final result.

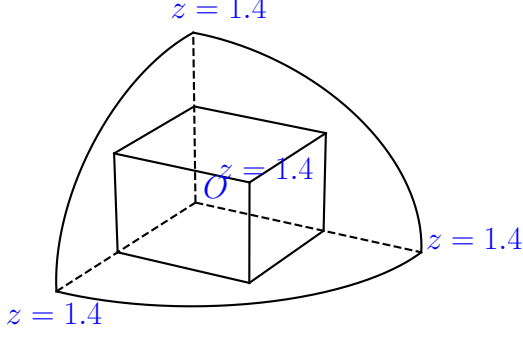


FIG. 4. Boxsize of the cube is $L = 3072/\sqrt{3} h^{-1} \text{Mpc} \sim 1774 h^{-1} \text{Mpc}$. Volume is $V = L^3 \sim 5.6 (h^{-1} \text{Mpc})^3$. Only one point in the cube can reach the redshift of 1.4, and $z = 0$ is at the origin O of the octant.

$2.9 \times 10^{10} h^{-1} M_{\odot}$ particle mass. Thus we have a number density of 3.4×10^{-3} particles/(Mpc/h) 3 , which is similar to Dark Energy Survey (DES) [33] full sample of galaxies. We use Nbodykit [34] to compute the modified matter density contrast field in Fourier space and get the estimated one using Eq. (29). Then we transform them back into real space and compare them in Fig. 5. The cube with volume $\sim 5.6 (h^{-1} \text{Gpc})^3$ is divided into 7^3 cells. Each row in Fig. 5 contains 7 panels; each panel is a slice through the simulation volume, $1774 h^{-1} \text{Mpc}$ wide, and one cell $\sim 253 h^{-1} \text{Mpc}$ thick. We can see that this estimator does an amazing job of extracting the large scale density job - we are able to reproduce almost every cell with large over- or under-densities, and the difference is apparently much smaller than the density field itself.

In Fig. 5, the left top cell of each row corresponds to the cell containing the origin ($z = 0$) in it; and the right bottom cell corresponds to the farthest cell from the origin ($z \sim 1.4$). We can use Fig. 6 to get a better view of this in a light cone, where in each row we still show the usual directly measure field $d_m^{\text{LC}}(\vec{r})$, estimated field $\hat{d}_m^{\text{LC}}(\vec{r})$ and their difference $(d_m^{\text{LC}} - \hat{d}_m^{\text{LC}})(\vec{r})$ respectively. We have two columns here, the left column shows cells near the origin and the right column shows cells far from the origin. While all the information in this figure is contained in Fig. 5, it still is a more straightforward way of expressing our result in a light cone.

Then we consider the halo catalog in the same light cone with halo masses between $2.2 \times 10^{12} h^{-1} M_{\odot} < M < 10^{14} h^{-1} M_{\odot}$ for brevity. We have similar results in other mass bins as well. We use Eq. (9) as the approximated matter density contrast, $\bar{n}_h(\vec{r})$ can be easily computed using halo positions and the Tinker bias function. We cut the whole light cone (the octant) into several slices and compute the mean density field \bar{n}_h and \bar{n}_h of each slice,

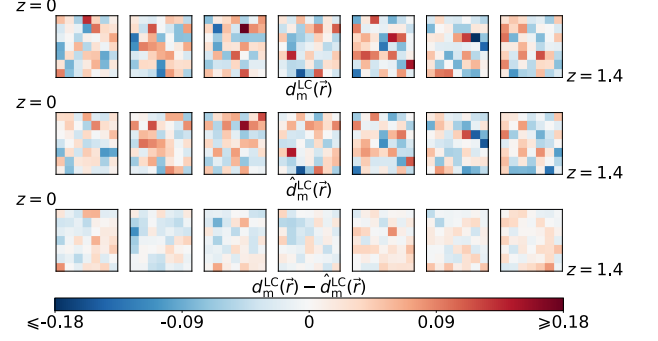


FIG. 5. Comparison of the true density field of the 1 in 700 matter particles of the Mice-GC simulation ($\delta_m^{\text{LC}}(\vec{r})$, top row) and the density field from the quadratic estimator ($\hat{\delta}_m^{\text{LC}}(\vec{r})$, middle row). The bottom row shows their difference. Each panel represents a slice through the simulation volume, $1774 h^{-1} \text{Mpc}$ wide, and one cell $\sim 253 h^{-1} \text{Mpc}$ thick. The integration range of \vec{k}_s is from $0.03 h \text{Mpc}^{-1}$ to $0.22 h \text{Mpc}^{-1}$.

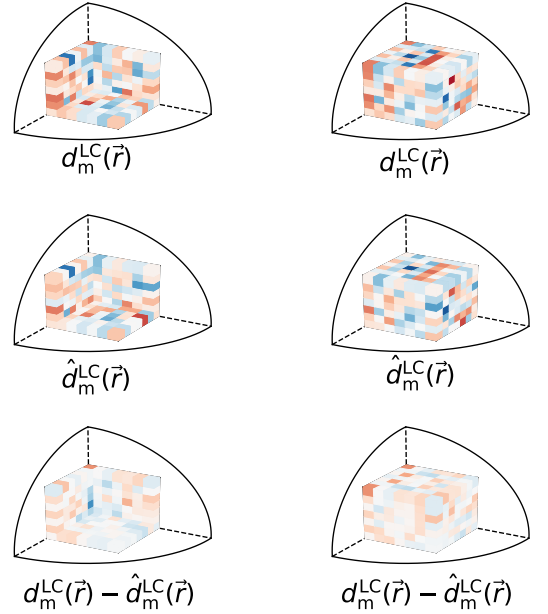


FIG. 6. Comparison of the true density field and the estimated density field of dark-matter-only catalog in a light cone with the same colorbar as Fig. 5. First row shows the modified matter density contrast near the origin (inner surfaces of the cube, $0 \leq z \lesssim 0.69$); second row shows the modified matter density contrast far from the origin (outer surfaces of the cube, $0.69 \lesssim z \lesssim 1.4$).

then get the mean field $\bar{n}_h(a(r))$ and $\bar{n}_h(a(r))$ at each position by interpolation. We compute the directly measured modified matter contrast $d_m^{\text{LC}}(\vec{r})$ and also the power spectrum in Fig. 3. The power spectrum perfectly characterizes linear matter power spectrum on large scales. We use the quadratic estimator Eq. (29) to get the reconstructed modified field and transform them back into real space. Again we have two similar plots Fig. 7 and Fig. 8. From Fig. 7 we can see that our quadratic estimator is still able to extract large scale information, especially large over- or under-density cells on first few low-redshift panels. The difference seems larger when we go higher into redshift, and we have the worst performance on the very right panel. We observe the same feature in Fig. 8 where the cells near the origin match each other better than cells far from the origin. The main reason for this effect is that nonlinear bias ($b_2, b_3 \dots$) becomes more important when we go deeper into the light cone [35].

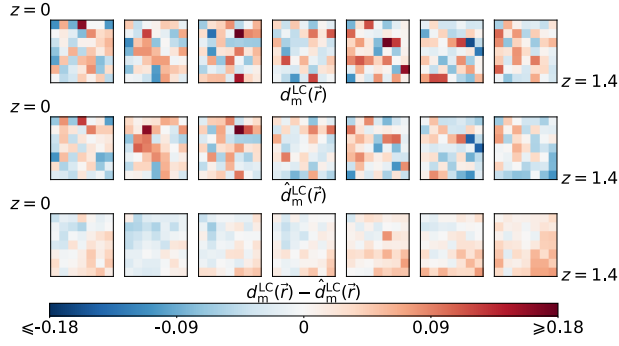


FIG. 7. Comparison of the true density field of the halo number density contrast in mass bin $2.2 \times 10^{12} h^{-1} M_\odot < M < 10^{14} h^{-1} M_\odot$ of the Mice-GC simulation ($\delta_m^{\text{LC}}(\vec{r})$, top row) and the density field from the quadratic estimator ($\hat{\delta}_m^{\text{LC}}(\vec{r})$, middle row) in the same light cone as Fig. 5, and their difference (bottom row). The integration range of \vec{k}_s is from $0.03 h \text{ Mpc}^{-1}$ to $0.35 h \text{ Mpc}^{-1}$. We use a larger upper limit to slightly reduce the noise term.

B. Redshift Space

Distribution of halos (and galaxies) is distorted and squashed observationally, when we use their redshift as an indicator of their radial distance due to halos' peculiar velocity. In the plane-parallel approximation, the mapping from real space to redshift space is given by [20]:

$$\vec{r}_{\text{rs}} = \vec{r} + \frac{(\vec{u} \cdot \hat{n})\hat{n}}{aH(a)} \quad (33)$$

where \vec{r}_{rs} is the redshift space coordinates, “rs” stands for “redshift space”, \vec{u} is the peculiar velocity field, \hat{n} is

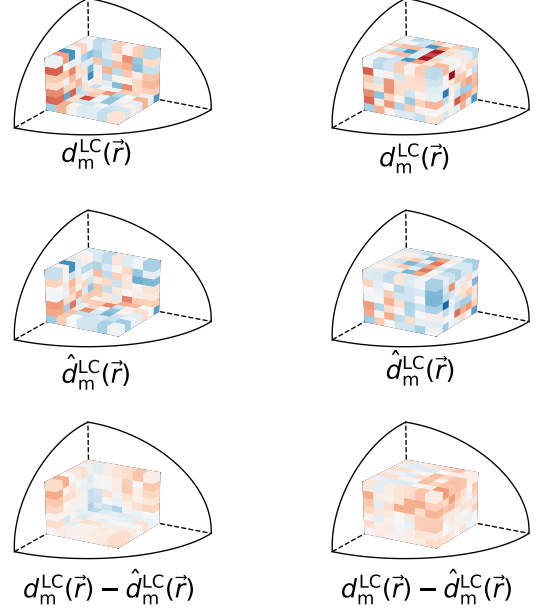


FIG. 8. Comparison of the true density field and the estimated density field of halo catalog in a light cone with the same colorbar as Fig. 5 (or Fig. 7). First row shows the modified matter density contrast near the origin (inner surfaces of the cube, $0 \leq z \lesssim 0.69$); second row shows the modified matter density contrast far from the origin (outer surfaces of the cube, $0.69 \lesssim z \lesssim 1.4$).

the direction of the line of sight and $H(a)$ is the Hubble parameter. Similarly, the matter density contrast in the redshift space can be written as a perturbative series:

$$\delta_{\text{m,rs}}(\vec{k}; a) = \sum_{n=1}^{\infty} \int \frac{d^3 \vec{k}_1}{(2\pi)^3} \cdots \int \frac{d^3 \vec{k}_n}{(2\pi)^3} \delta_{\text{D}}(\vec{k} - \vec{k}_1 - \cdots - \vec{k}_n) \times Z_n(\vec{k}_1, \dots, \vec{k}_n; a) \delta_{\text{m}}^{(1)}(\vec{k}_1; a) \cdots \delta_{\text{m}}^{(1)}(\vec{k}_n; a) \quad (34)$$

where

$$Z_1(\vec{k}; a) = 1 + f\mu^2 \quad (35)$$

$$Z_2(\vec{k}_1, \vec{k}_2; a) = F_2(\vec{k}_1, \vec{k}_2) + f\mu^2 G_2(\vec{k}_1, \vec{k}_2) + \frac{f\mu k}{2} \left[\frac{\mu_1}{k_1} (1 + f\mu_2^2) + \frac{\mu_2}{k_2} (1 + f\mu_1^2) \right] \quad (36)$$

with $\mu \equiv \vec{k} \cdot \hat{n}/k$ and $\mu_{1,2} \equiv \vec{k}_{1,2} \cdot \hat{n}/k_{1,2}$, and,

$$f(a) \equiv \frac{d \ln D_1(a)}{d \ln a} \quad (37)$$

$$G_2(\vec{k}_1, \vec{k}_2) = \frac{3}{7} + \frac{4}{7} \frac{(\vec{k}_1 \cdot \vec{k}_2)^2}{k_1^2 k_2^2} + \frac{\vec{k}_1 \cdot \vec{k}_2}{2k_1 k_2} \left[\frac{k_1}{k_2} + \frac{k_2}{k_1} \right] \quad (38)$$

The modified matter density contrast in the redshift space of a light cone can then be expressed as:

$$d_{\text{m,rs}}^{\text{LC}}(\vec{k}) = \int_V d^3\vec{r} \int \frac{d^3\vec{k}'}{(2\pi)^3} e^{i(\vec{k}' - \vec{k}) \cdot \vec{r}} \delta_{\text{m,rs}}(\vec{k}'; a(r)) \frac{D_{\text{ini}}}{D_1(a(r))} \quad (39)$$

One can prove that this definition still satisfies the relation (see appendix A for a detailed derivation):

$$\langle d_{\text{m,rs}}^{\text{LC}}(\vec{k}_s) d_{\text{m,rs}}^{\text{LC}}(\vec{k}'_s) \rangle|_{\vec{k}_s + \vec{k}'_s = \vec{k}_l} = f_{\text{rs}}(\vec{k}_s, \vec{k}'_s) d_{\text{m,rs}}^{\text{LC},(1)}(\vec{k}_l) \quad (40)$$

with

$$f_{\text{rs}}(\vec{k}_s, \vec{k}'_s) = 2C \frac{Z_1(\vec{k}_s; a(r \simeq L/2))}{Z_1(\vec{k}_s + \vec{k}'_s; a(r \simeq L/2))} \times \left[Z_2(-\vec{k}_s, \vec{k}_s + \vec{k}'_s; a=1) P_{\text{m,ini}}(k_s) + Z_2(-\vec{k}'_s, \vec{k}_s + \vec{k}'_s; a=1) P_{\text{m,ini}}(k'_s) \right] \quad (41)$$

where $L = 3072 h^{-1} \text{ Mpc}$ when we use MICE-GC simulation which is the depth of the simulation. It comes from the approximation when we take the ratio term out of the integrand. The redshift dependence of the f function is solved similarly as Eq. (24).

In Fig. 9 we use the halo catalog of MICE-GC simulation to reconstruct the monopole moment of the redshift space matter power spectrum.

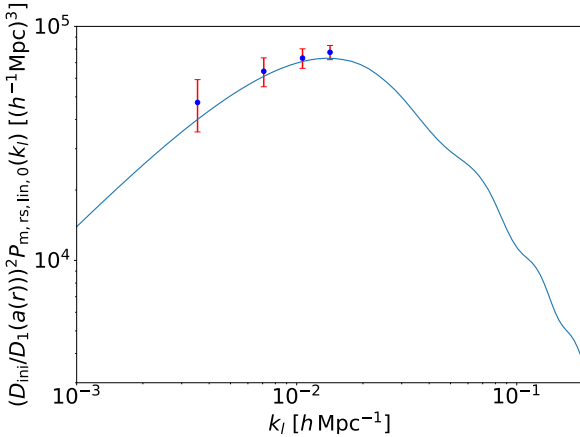


FIG. 9. Solid curve is the theoretical curve for the monopole moment of the linear redshift space matter power spectrum from Kaiser formula (detailed discussion in appendix A). Blue dots and their corresponding error bars are measured using the quadratic estimator in redshift space. The integration range for \vec{k}_s is from $0.03 h \text{ Mpc}^{-1}$ to $0.35 h \text{ Mpc}^{-1}$.

VII. CONCLUSION

ACKNOWLEDGMENTS

We thank Duncan Campbell for resourceful discussions. We also thank Enrique Gaztanaga for providing us with the 1 in 700 matter particles' positions of MICE-GC simulation. This work is supported by U.S. Dept. of Energy contract DE-SC0019248 and NSF AST-1909193. The BigMDPL simulation was performed at LRZ Munich within the PRACE project pr86bu. The CosmoSim database (www.cosmosim.org) providing the file access is a service by the Leibniz-Institute for Astrophysics Potsdam (AIP). This work has made use of CosmoHub. CosmoHub has been developed by the Port d'Informació Científica (PIC), maintained through a collaboration of the Institut de Física d'Altes Energies (IFAE) and the Centro de Investigaciones Energéticas, Medioambientales y Tecnológicas (CIEMAT), and was partially funded by the "Plan Estatal de Investigación Científica y Técnica y de Innovación" program of the Spanish government.

Appendix A: Proof of Eq. (40) in Redshift Space

One can prove that the leading order term of $d_{\text{m}}^{\text{LC}}(\vec{k})$ still characterizes the linear matter power spectrum in redshift space:

$$\begin{aligned} & \langle d_{\text{m}}^{\text{LC},(1)}(\vec{k}) d_{\text{m}}^{\text{LC},(1)}(\vec{k}') \rangle \\ &= (2\pi)^3 \delta_{\text{D}}(\vec{k} + \vec{k}') (1 + f(a=1)\mu^2)^2 P_{\text{m,ini}}(k) \\ &= (2\pi)^3 \delta_{\text{D}}(\vec{k} + \vec{k}') \left[\frac{D_{\text{ini}}}{D_1(a=1)} \right]^2 P_{\text{m,rs,lin}}(\vec{k}; a=1) \end{aligned} \quad (\text{A1})$$

where

$$P_{\text{m,rs,lin}}(\vec{k}; a) = (1 + f(a)\mu^2)^2 P_{\text{m,lin}}(k; a) \quad (\text{A2})$$

is the leading order redshift space matter power spectrum first derived by N. Kaiser [18]. We can decompose its direction-dependence by Legendre polynomials expansion as:

$$P_{\text{m,rs},\ell}(k; a) \equiv \frac{2\ell+1}{2} \int_{-1}^1 d\mu P_{\text{m,rs}}(\vec{k}; a) \mathcal{L}_{\ell}(\mu) \quad (\text{A3})$$

The monopole ($\ell = 0$) and the quadrupole ($\ell = 2$) moments have been measured in recent surveys [36]. Now we start our proof of Eq. (40), first we have:

$$\begin{aligned} & \langle \delta_{\text{m,rs}}^{(1)}(\vec{k}; a(r)) \delta_{\text{m,rs}}^{(2)}(\vec{k}'; a(r')) \rangle \\ &= Z_1(\vec{k}; a(r)) \langle \delta_{\text{m}}^{(1)}(\vec{k}; a(r)) \delta_{\text{m,rs}}^{(2)}(\vec{k}'; a(r')) \rangle \\ &= 2Z_1(\vec{k}; a(r)) \left[\frac{D_1(a(r'))}{D_{\text{ini}}} \right]^2 Z_2(-\vec{k}, \vec{k} + \vec{k}'; a(r')) \\ & \quad \times P_{\text{m,ini}}(k) \delta_{\text{m}}^{(1)}(\vec{k} + \vec{k}'; a(r)) \\ &= \frac{Z_1(\vec{k}; a(r))}{Z_1(\vec{k} + \vec{k}'; a(r))} \left\{ 2 \left[\frac{D_1(a(r'))}{D_{\text{ini}}} \right]^2 Z_2(-\vec{k}, \vec{k} + \vec{k}'; a(r')) \right. \\ & \quad \left. \times P_{\text{m,ini}}(k) \delta_{\text{m,rs}}^{(1)}(\vec{k} + \vec{k}'; a(r)) \right\} \end{aligned} \quad (\text{A4})$$

where in the step we use the first order expression of $\delta_{\text{m,rs}}$ in Eq. (34); and second step can be similarly derived as Eq. (23) with F_2 replaced by Z_2 ; and in the last step we use the expression again:

$$\delta_{\text{m,rs}}^{(1)}(\vec{k}; a(r)) = Z_1(\vec{k}; a(r)) \delta_{\text{m}}^{(1)}(\vec{k}; a(r)) \quad (\text{A5})$$

in order to get the similar expression as Eq. (23) in the braces. So when we evaluate $\langle d_{\text{m,rs}}^{\text{LC},(1)}(\vec{k}_s) d_{\text{m,rs}}^{\text{LC},(2)}(\vec{k}'_s) \rangle$ we

get an expression close to Eq. (26):

$$\begin{aligned} & \langle d_{\text{m,rs}}^{\text{LC},(1)}(\vec{k}_s) d_{\text{m,rs}}^{\text{LC},(2)}(\vec{k}'_s) \rangle \\ & \simeq 2C Z_2(-\vec{k}_s, \vec{k}_s + \vec{k}'_s; a=1) P_{\text{m,ini}}(k_s) \\ & \quad \times \int_V d^3\vec{r} \int \frac{d^3\vec{k}}{(2\pi)^3} \frac{Z_1(\vec{k} - \vec{k}'_s; a(r))}{Z_1(\vec{k}; a(r))} \frac{D_{\text{ini}}}{D_1(a(r))} \\ & \quad e^{-i(\vec{k} - \vec{k}_s - \vec{k}'_s)\vec{r}} \delta_{\text{m}}^{(1)}(\vec{k}; a(r)) \\ & \simeq \frac{Z_1(\vec{k}_s; a(r \simeq L/2))}{Z_1(\vec{k}_s + \vec{k}'_s; a(r \simeq L/2))} \\ & \quad \times 2C Z_2(-\vec{k}_s, \vec{k}_s + \vec{k}'_s; a=1) P_{\text{m,ini}}(k_s) d_{\text{m}}^{\text{LC},(1)}(\vec{k}_s + \vec{k}'_s) \end{aligned} \quad (\text{A6})$$

Z_2 is fixed at $a = 1$ when we use a similar approximation as Eq. (24). In order to recover $d_{\text{m}}^{\text{LC},(1)}(\vec{k}_s + \vec{k}'_s)$ from the integral, we also take the ratio $Z_1(\vec{k} - \vec{k}'_s; a(r))/Z_1(\vec{k}; a(r))$ out of the integrand by assuming that $\vec{k} = \vec{k}_s + \vec{k}'_s$ and $r = L/2$ where L is the depth of the survey. By performing these approximations we have proved Eq. (40).

Another interesting thing to notice in the redshift space construction is that, the Gaussian noise term \mathcal{A}_{rs} is direction-dependent following:

$$\mathcal{A}_{\text{rs}}(\vec{k}_l) \propto (1 + f(a=1)\mu_{k_l}^2) \quad (\text{A7})$$

One benefit we can take from this numerical result is that the projected detectability in redshift space still will not depend on the direction of \vec{k}_l . So the error bars will be the same for both real space and redshift space.

-
- [1] C. Modi, M. White, A. Slosar, and E. Castorina, *J. Cosmol. Astropart. P.* **11**, 023 (2019), [arXiv:1907.02330 \[astro-ph.CO\]](#).
 - [2] T. Baldauf, U. Seljak, L. Senatore, and M. Zaldarriaga, *J. Cosmol. Astropart. P.* **10**, 031 (2011), [arXiv:1106.5507 \[astro-ph.CO\]](#).
 - [3] D. Jeong and M. Kamionkowski, *Phys. Rev. Lett.* **108**, 251301 (2012), [arXiv:1203.0302 \[astro-ph.CO\]](#).
 - [4] Y. Li, W. Hu, and M. Takada, *Phys. Rev. D* **90**, 103530 (2014), [arXiv:1408.1081 \[astro-ph.CO\]](#).
 - [5] H.-M. Zhu, U.-L. Pen, Y. Yu, X. Er, and X. Chen, *Phys. Rev. D* **93**, 103504 (2016), [arXiv:1511.04680 \[astro-ph.CO\]](#).
 - [6] A. Barreira and F. Schmidt, *J. Cosmol. Astropart. P.* **06**, 03 (2017), [arXiv:1703.09212 \[astro-ph.CO\]](#).
 - [7] P. Li, S. Dodelson, and R. A. C. Croft, *Phys. Rev. D* **101**, 083510 (2020), [arXiv:2001.02780 \[astro-ph.CO\]](#).
 - [8] A. V. Kravtsov and A. Klypin, Anatoly, *Astrophys. J.* **520**, 437 (1999), [arXiv:astro-ph/9812311 \[astro-ph\]](#).
 - [9] V. Desjacques, D. Jeong, and F. Schmidt, *Phys. Rept.* **733**, 1 (2018), [arXiv:1611.09787 \[astro-ph.CO\]](#).
 - [10] LSST Dark Energy Science Collaboration, [arXiv:1211.0310 \[astro-ph.CO\]](#).
 - [11] WFIRST Science Definition Team, [arXiv:1208.4012 \[astro-ph.IM\]](#).
 - [12] DESI Collaboration, [arXiv:1907.10688 \[astro-ph.IM\]](#).
 - [13] U. Seljak, A. Makarov, R. Mandelbaum, C. M. Hirata, N. Padmanabhan, P. McDonald, M. R. Blanton, M. Tegmark, N. A. Bahcall, and J. Brinkmann (SDSS Collaboration), *Phys. Rev. D* **71**, 043511 (2005), [arXiv:astro-ph/0406594](#).
 - [14] C. Chang *et al.* (DES Collaboration), *Mon. Not. Roy. Astron. Soc.* **459**, 3203 (2016), [arXiv:1601.00405 \[astro-ph.CO\]](#).
 - [15] J. Prat *et al.* (DES Collaboration), *Mon. Not. Roy. Astron. Soc.* **473**, 1667 (2018), [arXiv:1609.08167 \[astro-ph.CO\]](#).
 - [16] S. M. Carroll, [arXiv:gr-qc/9712019 \[gr-qc\]](#).
 - [17] M. Troxel *et al.* (DES Collaboration), *Phys. Rev. D* **98**, 043528 (2018), [arXiv:1708.01538 \[astro-ph.CO\]](#).
 - [18] N. Kaiser, *Mon. Not. Roy. Astron. Soc.* **227**, 1 (1987).
 - [19] B. Jain and E. Bertschinger, *Astrophys. J.* **431**, 495 (1994), [arXiv:astro-ph/9311070 \[astro-ph\]](#).
 - [20] F. Bernardeau, S. Colombi, E. Gaztañaga, and Scoccimarro, *Phys. Rept.* **367**, 1 (2012), [arXiv:astro-ph/0112551 \[astro-ph\]](#).
 - [21] R. Takahashi, *Prog. Theor. Phys.* **120**, 549–559 (2008), [arXiv:0806.1437 \[astro-ph.CO\]](#).
 - [22] U. Seljak and M. S. Warre, *Mon. Not. Roy. Astron. Soc.* **355**, 129 (2004), [arXiv:astro-ph/0403698 \[astro-ph\]](#).
 - [23] S. Bhattacharya, K. Heitmann, M. White, Z. Lukić, C. Wagner, and S. Habib, *Astrophys. J.* **732**, 122 (2011), [arXiv:1005.2239 \[astro-ph.CO\]](#).
 - [24] J. L. Tinker, B. E. Robertson, A. V. Kravtsov, A. Klypin, M. S. Warren, G. Yepes, and S. Gottlober, *Astrophys. J.* **724**, 878 (2010), [arXiv:1001.3162 \[astro-ph.CO\]](#).
 - [25] W. J. Percival *et al.*, *Astrophys. J.* **657**, 645 (2007), [arXiv:astro-ph/0608636 \[astro-ph\]](#).
 - [26] P. Fosalba, M. Crocce, E. Gaztañaga, and F. J. Castander, *Mon. Not. Roy. Astron. Soc.* **460**, 3624–3636 (2015), [arXiv:1512.07295 \[astro-ph.CO\]](#).
 - [27] J. G. Cresswell and W. J. Percival, *Mon. Not. Roy. Astron. Soc.* **392**, 682 (2008), [arXiv:0808.1101 \[astro-ph\]](#).
 - [28] A. Klypin, G. Yepes, S. Gottlober, F. Prada, and S. Hess, *Mon. Not. Roy. Astron. Soc.* **457**, 4340 (2014), [arXiv:1411.4001 \[astro-ph.CO\]](#).
 - [29] Planck Collaboration, *Astron. Astrophys.* **571**, 66 (2014), [arXiv:1303.5076 \[astro-ph.CO\]](#).
 - [30] P. S. Behroozi, R. H. Wechsler, and H.-Y. Wu, *Astrophys. J.* **762**, 109 (2013), [arXiv:1110.4372 \[astro-ph.CO\]](#).
 - [31] P. Fosalba, M. Crocce, E. Gaztañaga, and F. J. Castander, *Mon. Not. Roy. Astron. Soc.* **448**, 2987 (2015), [arXiv:1312.1707 \[astro-ph.CO\]](#).
 - [32] M. Crocce, F. J. Castander, E. Gaztañaga, P. Fosalba, and J. Carretero, *Mon. Not. Roy. Astron. Soc.* **453**, 1513 (2015), [arXiv:1312.2013 \[astro-ph.CO\]](#).
 - [33] Dark Energy Survey Collaboration, *Mon. Not. Roy. Astron. Soc.* **460**, 1270–1299 (2016), [arXiv:1601.00329 \[astro-ph.CO\]](#).
 - [34] N. Hand, Y. Feng, F. Beutler, Y. Li, C. Modi, U. Seljak, and Z. Slepian, *Astrophys. J.* **156**, 160 (2018), [arXiv:1712.05834 \[astro-ph.CO\]](#).
 - [35] T. Lazeyras, C. Wagner, T. Baldauf, and F. Schmidt, *J. Cosmol. Astropart. P.* **02**, 018 (2016), [arXiv:1511.01096 \[astro-ph.CO\]](#).
 - [36] H. Gil-Marín *et al.*, *Mon. Not. Roy. Astron. Soc.* **460**, 4188 (2016), [arXiv:1509.06386 \[astro-ph.CO\]](#).